POLITECNICO DI TORINO
Repository ISTITUZIONALE

Synergistic surface engineering of PBF-EB/M Ti–6Al–2Sn–4Zr–2Mo: linking support-fingerprint morphology to high-temperature tribological behavior

Original
Synergistic surface engineering of PBF-EB/M Ti–6Al–2Sn–4Zr–2Mo: linking support-fingerprint morphology to high-temperature tribological behavior / Davoodi, F., Moazzen, P., Taghian, M., Galati, M., Mohammadi, M., Saboori, A.. - In: PROGRESS IN ADDITIVE MANUFACTURING. - ISSN 2363-9512. - 11:6(2026), pp. 5935-5954. [10.1007/s40964-026-01677-w]

Availability:
This version is available at: 11583/3013017 since: 2026-07-13T09:22:26Z

Publisher:
Springer Nature

Published
DOI:10.1007/s40964-026-01677-w

Terms of use:

This article is made available under terms and conditions as specified in the corresponding bibliographic description in the repository

Publisher copyright

(Article begins on next page)

21 November 2026

Progress in Additive Manufacturing (2026) 11:5935–5954
https://doi.org/10.1007/s40964-026-01677-w

RESEARCH

Synergistic surface engineering of PBF-EB/M Ti–6Al–2Sn–4Zr–2Mo: linking support-fingerprint morphology to high-temperature tribological behavior

Farideh Davoodi[1,2] · Parisa Moazzen[3] · Mohammad Taghian[4,5] · Manuela Galati[4,5] · Mohsen Mohammadi[3] · Abdollah Saboori[4,5]

Received: 30 January 2026 / Accepted: 24 March 2026 / Published online: 14 April 2026
© The Author(s) 2026

Abstract

This study investigated the effects of two industrialized post-surface treatments, grinding, and grinding-tumble finishing, on the tribological behaviour of Ti–6Al–2Sn–4Zr–2Mo (Ti6242) samples produced via Powder Bed Fusion-Electron Beam/Metal (PBF-EB/M), focusing on surfaces that retain the characteristic fingerprint of support structures. By employing a combination of grinding and tumble finishing, this research aimed to mitigate the negative effects of surface irregularities, enhance wear resistance, reduce friction, and, consequently, make these components suitable for demanding applications such as aerospace engine and turbine components, where high temperatures and frictional stresses are critical. Friction tests were conducted from room temperature to 450 °C, complemented by nanoindentation, surface roughness, and microhardness analyses. The combination of grinding and tumble finishing resulted in a ~ 10% increase in hardness and improved the hardness-to-elastic modulus ratio compared to grinding alone. Interestingly, although the hybrid-treated surfaces exhibited slightly higher surface roughness (*Ra*) than the ground samples, they demonstrated superior tribological performance at room temperature. This hybrid treatment also reduced the friction coefficient at 450 °C, which may be attributed to the formation of titanium oxide, which enhances lubrication. The study demonstrated the effectiveness of the combined treatments in mitigating the negative impact of support structure features on the tribological performance of the final components.

Keywords Additive manufacturing · Ti6242 alloy · Powder Bed Fusion-Electron Beam/Metal (PBF-EB/M) · Surface treatment · Tribological behavior · Surface topography

✉ Abdollah Saboori
abdollah.saboori@polito.it

Farideh Davoodi
farideh.davoodi@poliba.it

Parisa Moazzen
parisa.moazzen@unb.ca

Mohammad Taghian
mohammad.taghian@polito.it

Manuela Galati
manuela.galati@polito.it

Mohsen Mohammadi
Mohsen.Mohammadi@unb.ca

[1] Polytechnic University of Bari, Bari, Italy

[2] Institute for Advanced Manufacturing (KSF), Furtwangen University, Furtwangen im Schwarzwald, Germany

[3] University of New Brunswick, Fredericton, Canada

[4] Department of Management and Production Engineering, Polytechnic University of Turin, Turin, Italy

[5] Integrated Additive Manufacturing Center (IAM@PoliTo), Polytechnic University of Turin, Turin, Italy

1 Introduction

Ti–6Al–2Sn–4Zr–2Mo (Ti6242) is a near-α titanium alloy specifically developed to withstand higher temperatures compared to Ti6Al4V, which is one of the most common titanium alloys [1]. Moreover, Ti6242 exhibits high uniaxial tensile and toughness properties as well as exceptional creep, fatigue, and corrosion resistance. These properties make this alloy a promising candidate for aerospace and power generation components, such as compressor disks, compressor blades, turbine casings, and structural components operating in elevated-temperature sections of gas-turbine engines [2, 3]. Considering its application in high-temperature environments, the tribological response of Ti6242 is an important aspect that remains relatively underexplored in the literature. Among the limited studies available, Heilig et al. [4] studied the dry sliding wear behavior of Ti6242 at elevated temperatures up to 800 °C. Their results showed that the coefficient of friction (COF) increased with increasing temperature, while the wear volume decreased up to about 600 °C due to the formation of a protective oxide-based mechanically mixed layer on the wear track.

The exceptional properties of Ti6242 are largely controlled by its microstructure, particularly the distribution of the α and β phases, which evolve during processing and influence the material's mechanical and thermal performance [5]. However, producing Ti6242 components through conventional manufacturing processes faced several challenges [6]. For instance, the traditional casting process for this alloy often results in internal defects within the casting microstructures, such as porosity and inhomogeneous grain structures, consequently undermining the overall mechanical properties. On the other hand, the high-temperature strength of the Ti6242 alloy makes it very difficult to machine through subtractive manufacturing processes. This challenge comes back to the rapid degradation of the cutting-edge of the tool during the material removal [7, 8]. Therefore, several efforts have been made so far to overcome these challenges and broaden the applications of Ti6242 alloy in various industries.

As one of the promising solutions, additive manufacturing (AM) techniques have revolutionized the production of complex components with enhanced design flexibility and reduced lead times [9, 10]. Among recent studies exploring additively manufactured titanium alloys, Praveenkumar et al. [11] investigated the tribological performance of L-PBF Ti6Al4V alloy from room temperature up to 450 °C, showing that the native oxide layer reduced adhesive wear at ambient conditions, while at elevated temperatures the formation of tribo-oxide layers and oxidized debris promoted oxidative and abrasive wear mechanisms.

Among the various AM technologies, Powder Bed Fusion – Electron Beam/Metal (PBF-EB/M), has garnered significant attention [12, 13]. This technique utilizes an electron beam as a power source and is uniquely capable of producing metallic components at high temperatures under a vacuum environment that prevents oxidation and minimizes residual stress formation [14, 15]. Nevertheless, it is well documented that the as-built parts produced via PBF-EB/M suffer from poor surface quality and dimensional accuracy [16]. As a matter of fact, it is reported that increasing the surface roughness can reduce the wear resistance of the components significantly [17, 18]. Consequently, post-processing treatments are required to attain specific surface morphologies and geometric tolerances that are challenging to achieve solely through AM technologies [19]. To improve the surface characteristics of AM components, a range of post-processing treatments is reported, including turning [20], peening [21], coatings [22], milling [23], chemical treatment [24], blasting [25], and tribo-finishing methods [17, 26].

In addition to improving surface roughness, post-processing and surface modification treatments can significantly influence the tribological performance of titanium alloys, particularly under elevated temperature conditions. For example, Zeng et al. [27] reported that thermal oxidation treatment can effectively enhance the wear resistance of Ti6Al4V by forming a hard TiO_2 surface layer. Their results showed that the oxidation temperature strongly affects the tribological response, where samples oxidized at 700 °C exhibited the best wear resistance. Similarly, Naghian et al. [28] investigated the wear behavior of PBF-EB/M Ti6242 subjected to different heat treatments and demonstrated that post-treatment significantly alters the microstructure and consequently the dominant wear mechanisms. In particular, heat treatment at 960 °C resulted in the best wear resistance.

Tribo-finishing, also known as tumble finishing, is an advanced surface finishing technique that improves surface quality by utilizing the flow of abrasive media, sometimes combined with chemical agents, while rotating at varying speeds inside a tank [29]. This process offers several advantages, including cost-effectiveness and short processing time. Its low costs arise from a straightforward setup and reduced labour requirements, making it a promising and economical solution for industrial applications. Recently, tumble finishing has been used in a few studies as a post-processing step to improve the surface quality of the AM parts. For example, in the study by Benedetti et al. [30], tumble finishing of laser powder bed fusion (L-PBF)-Ti6Al4V samples resulted in a reduction of surface porosity and roughness, along with an increase in compressive residual stress. In another attempt, they found that applying tumble finishing to as-built Ti6Al4V samples produced via

L-PBF reduced the surface roughness (*Sa*) by 12%. Moreover, they revealed that this surface treatment significantly enhanced fatigue life, with an increase of up to 1.6 times at a constant maximum stress of 300 MPa [31].

It should be underlined that all these previous works have been focused on improving the up-skin surfaces by applying tumble finishing. However, the external surface of the metallic components produced via AM also includes the interface between the part and support structure, which can have a worse surface quality with respect to the up-skin surfaces. In fact, the support structures in the PBF-EB/M process play a critical role in ensuring the successful production of complex geometries. These structures are used to prevent overhangs, and distortions. In the case of overhangs, support structures proves a foundation for them and let the materials to cool and solidify without drooping. Moreover, they are used as heat conductor so as to dissipate the heat and avoid the local heat accumulation that can result in alloying element evaporation. On the other hand, support structures provide mechanical support and help maintain the shape and integrity of the part during the PBF-EB/M process. Despite all these critical roles, they also increase the build time and material consumption and deteriorate the surface quality in their interface with the component that needs longer and dedicated post-processing treatment. Therefore, a careful design should be undertaken to minimize the support structure quantity and its relevant drawbacks and increase the building efficiency.

Despite extensive research on the additive manufacturing of titanium alloys, the surface condition of support-affected regions in PBF-EB/M processed Ti6242 components has remained largely unexplored. While previous studies have primarily focused on improving the quality of up-skin surfaces, support-contact regions pose additional challenges. While there is literature investigating the influence of support structures on global surface roughness [32], down-facing regions, and residual stresses [33] in powder-bed fusion parts, systematic investigations specifically addressing the surface morphology and tribological behavior of the support-contact interface remain very limited. To the best of the authors' knowledge, a dedicated tribological assessment of this support fingerprint region has not yet been comprehensively reported. Therefore, it is essential to evaluate this aspect and assess the efficiency of two industrial post-processing methods in improving the surface quality of these regions. Furthermore, there is a noticeable lack of research examining the tribological behavior of PBF-EB/M fabricated Ti6242 alloy. Accordingly, this study aims to fill this gap by investigating, for the first time, the combined influence of two industrial surface finishing treatments and temperature on the wear resistance and mechanical properties of the support-contact surfaces in Ti6242 components.

2 Materials and methods

2.1 Sample production

A gas-atomized spherical Ti–6Al–2Sn–4Zr–2Mo alloy powder supplied by TLS Technik GmbH & Co. was used as a starting material in this work. In order to analyze the morphology and chemical composition of the starting powder, scanning electron microscopy (SEM, PhenomX) equipped with an energy-dispersive X-ray spectroscopy (EDS) analysis system was utilized. The results were confirmed by ICP (inductively coupled plasma) analysis (Avio 500 ICP-OES, PerkinElmer), combined with inert gas fusion (ONH836 analyzer, LECO Europe BV) and presented in Table 1. According to the oxygen content analysis of the starting powder in Table 1, it contains a low oxygen level. The initial powder utilized in this study was characterized by particles with a diameter ranging from 45 to 106 µm and a volume median diameter of around 75 µm. Figure 1a depicts the SEM micrographs of the initial Ti6242 powder, predominantly spherical, alongside some agglomerates. Additionally, a notable portion of the particles exhibited satellite coverage, along with some particles, including internal porosity. It is widely acknowledged that the presence of such defects can impede powder flowability and the final quality of the as-built samples [6]. Consequently, larger outlet windows were employed during machine setup to mitigate this powder regulation issue.

An Arcam A2X PBF-EB/M machine was used to fabricate the specimens with the standard parameters, including a 60 kV accelerating voltage, a 50 µm layer thickness, and software version 5.2.52. The PBF-EB/M process was carried out using a beam speed of 1060 mm/s, a reference current of 6 mA, a focus offset of 10 mA, and a line offset of 0.2 mm. The cylindrical samples, measuring 30 ± 0.03 mm in diameter and 5 ± 0.03 mm in height, designated for the wear test, were fabricated horizontally in an x-y plane (Fig. 1b, c). They were positioned 10 ± 0.1 mm above the starting plate, and the samples were connected to the starting plate using the standard thin wafer supports. Before applying the first layer of powder, the stainless-steel starting plate was subjected to preheating through electron beam

Table 1 Chemical composition of the starting Ti6242 powder

Chemical composition (wt%)	Al	Zr	Sn	Mo	Si	O	Ti
EDS analysis	5.94	4.00	2.19	2.01	0.15	–	Bal.
ICP-Inert gas fusion	6.05	3.34	1.70	1.62	0.06	0.13	Bal.

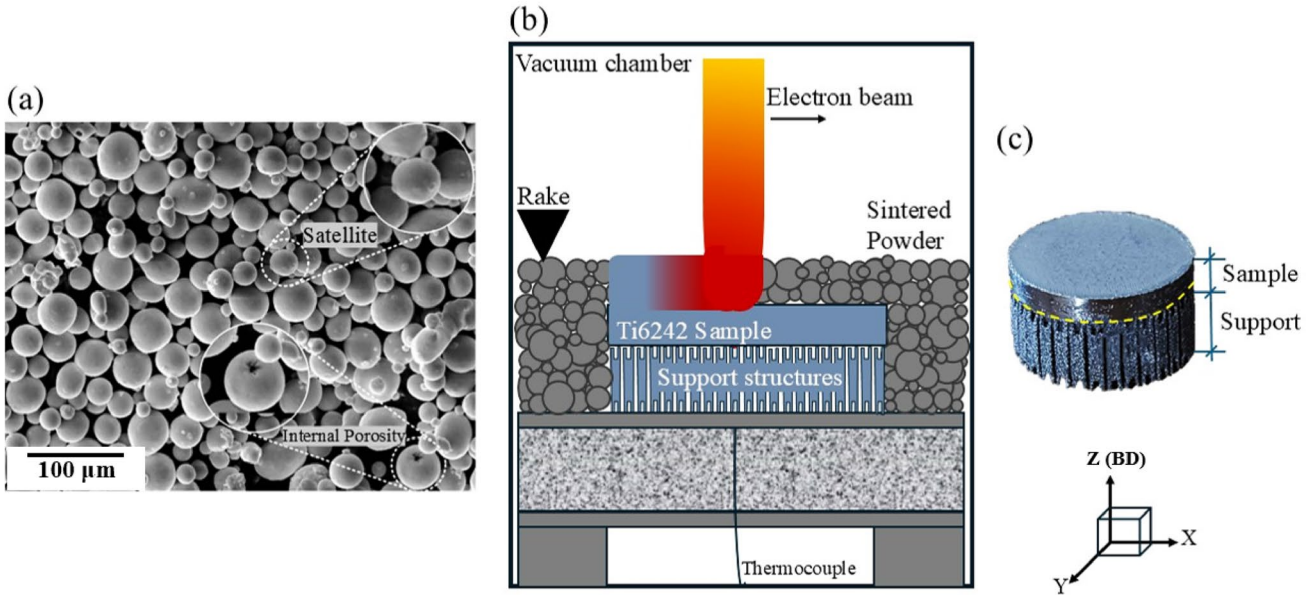


Fig. 1 **a** SEM micrograph of the starting Ti6242 powder, **b** schematic of the PBF-EB/M build chamber, and **c** A view of the as-built Ti6242 sample

scanning, reaching a temperature of 700 °C. Subsequently, a layer of powder was evenly distributed onto the preheated starting plate, and the preheating phase of the powder commenced before the melting step. This preheating of the powder before fusion was replicated for each subsequent layer until the completion of the manufacturing process. Once the fabrication was finalized, any residual unmelted powder was effectively removed from the samples using a Powder Removal System, employing compressed air and the same powder as the media.

2.2 Post-processing treatments

Grinding and a hybrid post-treatment combining grinding with tumble finishing were employed to improve the surface quality of the as-built Ti6242 alloys. From here onwards, the samples are named AB (as-built), G (post-treated by grinding), and G+TF (post-treated by grinding and tumble finishing).

Before the post-processing processes, all the wafer supports were removed from the specimens to study the surface, including the fingerprints of the support structures. In the single grinding process, the samples were effectively polished using SiC abrasive papers ranging from grit size 180# to 1200#, in accordance with the standards set by the Federation of European Producers of Abrasives (FEPA). To prepare the samples for the G+TF treatment, they were initially ground to achieve a surface roughness of around 1 µm. Following this, TF was conducted using 6×6 EVO triangular ceramic granules inside a 100-L circular vibrating barrel provided by SILCO s.r.l. The rotating speed was set at 200 revolutions.min^{-1}, lasting 2 h. A visual depiction of the TF machine is provided in Fig. 2. Continuous impact between the abrasive products and the treated pieces effectively removes the ribs, resulting in an optimal finish.

2.3 Material characterization

To examine the defects and porosities in as-built Ti6242 specimens, an X-ray CT scanner (GE Phoenix v|tome|x S240 system) was used. It equipped with a 180 kV/20 W high-power nanofocus X-ray tube, allowed for high-resolution imaging with a pixel size of 100 µm. The images were produced with a resolution of 2500 × 3000 pixels.

The microstructural characterization of the samples was conducted using an FEI Scios 2 focused ion/SEM dual beam instrument equipped with a high-resolution Oxford Symmetry® S3 electron backscatter diffraction (EBSD) detector (1244 × 1024 pixels, CMOS sensor), integrated with AZtec-HKL software. EBSD data analysis and post-processing, including grain size measurement, crystallographic orientation mapping, and morphological evaluation, were carried out using AztecAzflex Oxford software (version 5.1).

An RTP-80 profilometer with a TL90 drive unit was employed to measure the surface roughness of the samples in different states. Mean values for surface roughness were derived from five measurements conducted on each specimen.

A Vickers microhardness tester was used to analyze the microhardness of the samples on their cross-section (x–z plane) using a diamond Vickers indenter (Qness Q10 Microhardness tester). A constant load of 0.5 N was applied for 15 s. The measurements were taken at various zones, and

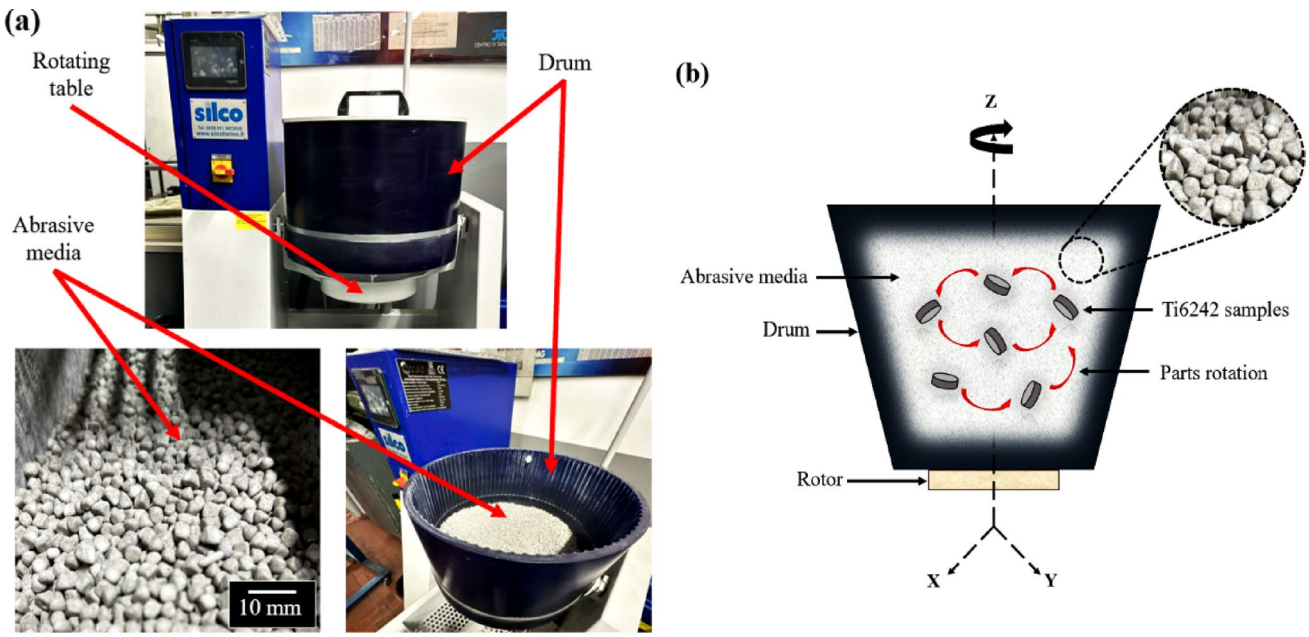


Fig. 2 **a** Tumble finishing (TF) machine and abrasive media, and **b** schematic illustration for the TF treatment of As-built (AB) Ti6242 samples

the average values of five measurements were recorded and reported.

The elastic modulus, nano hardness, and loading-unloading curves of the specimens were measured by using an NHT2 CSM Instruments nanoindentation tester equipped with a Berkovich indenter under a maximum load of 10 mN. Each test was repeated three times, and the average values of the elastic modulus and hardness were reported.

Dry sliding wear tests were conducted on Ti6242 discs with a diameter of 30 mm using a ball-on-disc CSM high-temperature wear tester. The tests were performed on the flat circular face of the cylindrical specimens, corresponding to the x–y plane of the build direction, which represents the downskin region originally connected to the support structures during the PBF-EB/M process and constitutes the main focus of the present study. The experiments were carried out at room temperature, as well as at 250 °C and 450 °C. Other test conditions were as follows: Load = 5 N (a maximum contact pressure approximately reaching 825.64 MPa according to the Hertzian contact stress model.), sliding velocity = 0.1 ms^{-1}, and test duration = 30 min. The selected parameters were adopted in line with previous tribological studies on titanium alloys under comparable dry sliding conditions [34], ensuring stable and reproducible wear behavior for comparative analysis.

Each experiment was performed three times to ensure reproducibility. An alumina (Al_2O_3) ball with a diameter of 10 mm and a hardness of ~ 18.5 GPa was selected as hard, and wear and thermal-resistant counterpart. Al_2O_3 balls are widely used in tribological studies of titanium alloys, enabling reliable comparison with existing literature [35, 36]. After the tests, the morphology of the worn surfaces was examined using a Philips XL30-SEM-EDS analysis.

Furthurmore, an X-ray diffractometer (XRD) (ASENWARE, AW-XDM300) was employed to examine the phase composition of the samples after the wear tests. The X-rays were produced using a Cu target at 40 kV and 30 mA, covering a scanning angular range of 20° to 90° with a step size of 0.05° and a step time of 1 s. Before any analysis, the samples were cleaned in an ethanol ultrasonic bath for 10 min, rinsed with distilled water for 5 min, and dried afterwards.

3 Results and discussion

3.1 Microstructural characteristics

It is generally believed that the presence of porosity in the metallic component deteriorates its mechanical performance and load-bearing capacity [37, 38]. The porosity content of the as-built Ti6242 samples was evaluated via X ray computer tomography (XCT) analysis to assess how the manufacturing process affected internal defect. These defects are known to influence mechanical properties such as wear resistance and hardness. The outcome of this analysis is presented in Fig. 3, where the pores are color-coded by their diameter. The results clearly confirmed that the porosity content of the as-built Ti6242 alloy was negligible, and the samples were successfully manufactured with a relative density of 99.95%. The maximum detected pore size was below 0.15 mm (150 µm), further supporting the high densification level of the material. The absence of significant

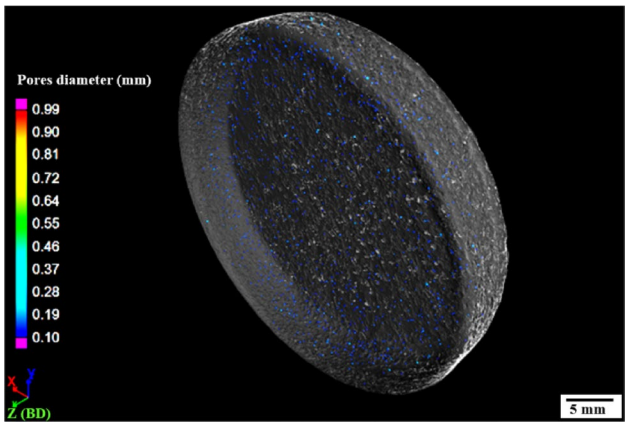


Fig. 3 Porosity analysis of an as-built Ti6242 sample via X-ray CT analysis

porosity suggests that the PBF-EB/M process was successful in producing components with high structural integrity, minimizing the impact of internal defects on the mechanical properties. However, the surface regions, particularly those connected to support structures, are more prone to surface irregularities and roughness, necessitating further post-processing to improve their tribological performance.

Figure 4 illustrates the microstructure of the Ti6242 alloy, featuring a basketweave pattern of α + β phases. This microstructure results from the repeated heating cycles caused by the upper sintered layers and the heat influence from the powder bed during the PBF-EB/M process. These thermal conditions promote the partial transformation of the α' martensitic phase into the α phase within the existing β grains. The interaction of α laths nucleating within prior β grains forms the characteristic interwoven morphology. Consequently, a primary Widmanstätten microstructure forms, characterized by a basketweave structure with α colonies concentrated near the boundaries of the β grains [6, 39], as shown in Fig. 4a and b. The distinct microstructure indicating fine α + β grains contributes to the ductility of the PBF-EB/M components, making them comparable to their wrought counterparts [40].

For a more detailed examination of the microstructure, Fig. 5 presents the EBSD results for the untreated downskin surface (Fig. 5a), the cross-section near the upskin (Fig. 5b), and the cross-section near the downskin after tumble finishing (Fig. 5c). A clear difference in microstructural features is observed between the untreated and treated conditions. The Inverse pole figure (IPF) map of the tumble-finished sample reveals a markedly refined microstructure, particularly in the near-surface region. This observation can be primarily attributed to the mechanical action of the tumbling process, which induces localized plastic deformation due to repeated impacts and surface friction.

These cyclic stresses activate multiple slip systems in the α-Ti matrix, generating a high dislocation density that subdivides the original α grains into smaller dislocation cells and subgrains. With continued impacts, these substructures evolve into refined, equiaxed domains through dynamic recovery and polygonization. Although the overall temperature during tumbling remains low, the accumulated strain energy is sufficient to drive partial rearrangement of dislocations without full recrystallization, resulting in a finer and more misoriented surface microstructure [29].

The grain size distribution graphs indicate a reduction in the grain diameter from approximately 5 µm in the untreated condition to about 3 µm after tumbling. In regions exhibiting a basket-weave morphology, α-laths appear interwoven and the boundaries between α-colonies are not clearly

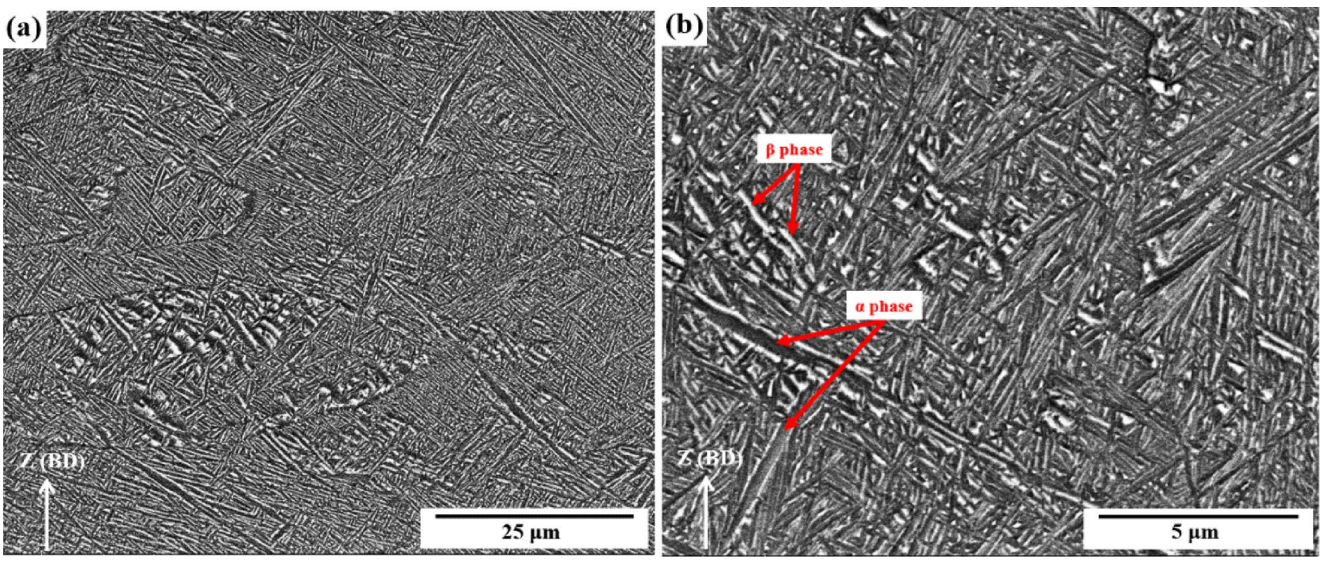


Fig. 4 SEM micrograph of the Ti6242 sample in the as-built condition, showing the basketweave microstructure at two magnifications. **a** Low-magnification image showing the overall pattern of the α+β phases, and **b** high-magnification micrograph revealing finer microstructural details

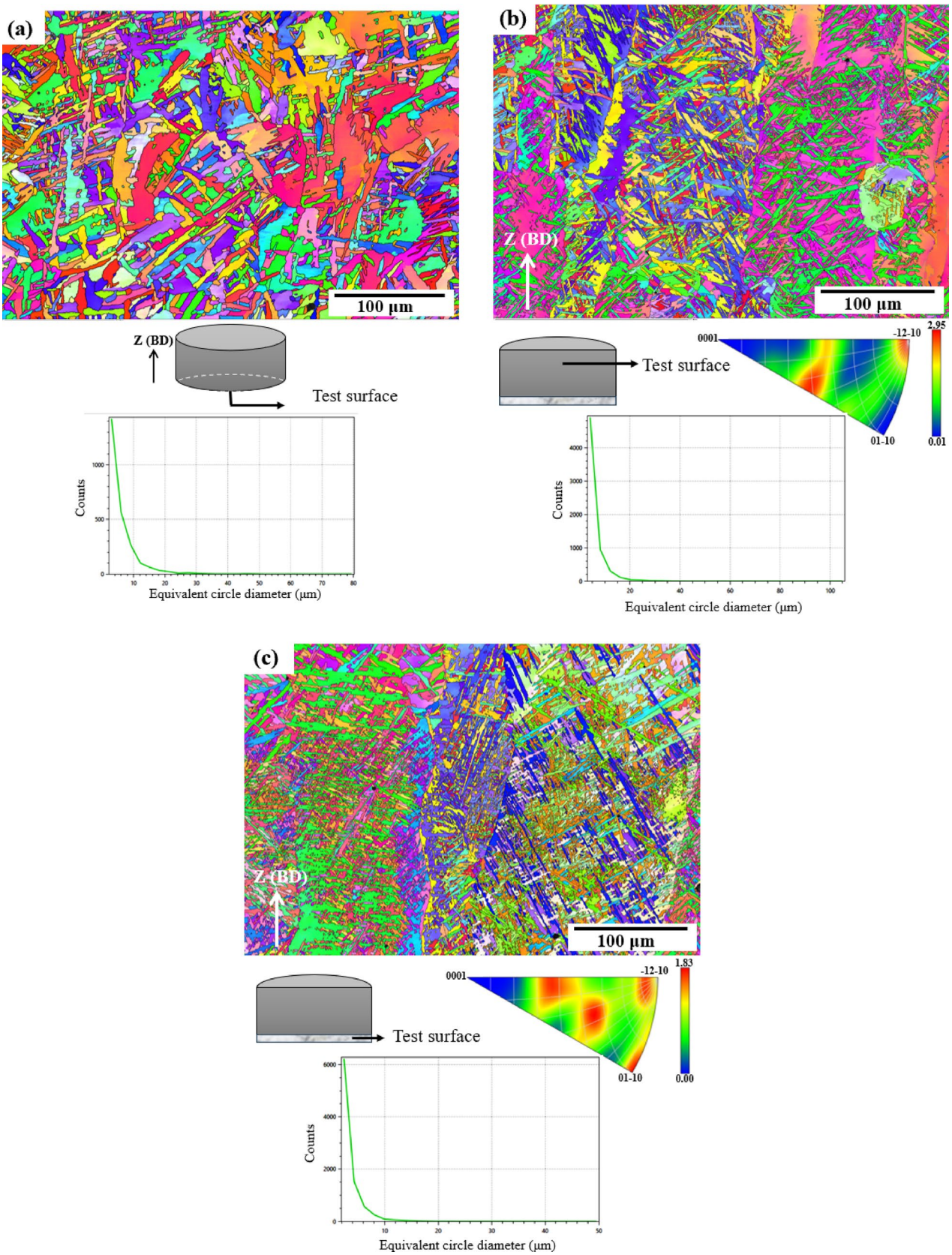


Fig. 5 Inverse pole figure (IPF) maps of the Ti6242 sample showing, **a** the untreated downskin surface, **b** the cross-section near the upskin, and **c** the cross-section near the downskin following tumble finishing

distinguishable. The inverse pole figure parallel to the build direction (z) of the as-built PBF-EB/M Ti6242 surface exhibits a dominant <–12–10>fiber component, accompanied by a secondary orientation close to <01–11>with an angular deviation of approximately 3°. This dual-component texture indicates the coexistence of multiple prismatic variants that developed due to slight variations in the solidification path and local lattice rotations during the β→α transformation. After tumbling, the overall texture intensity decreases markedly; however, the orientation maxima shift toward <01–10>and <–15–43>directions, deviated by about 2.77°. These new orientations reflect the partial reorientation of surface α grains caused by multidirectional micro-impacts and plastic shear during tumbling. The appearance of these slightly misoriented components, together with the reduced texture sharpness, confirms the occurrence of local lattice rotations and orientation spread confined to the near-surface layer, while the underlying bulk retains the original<10–10>fiber texture. Although tumble finishing primarily affects the outermost layers and does not significantly alter the bulk material, these localized changes can enhance mechanical properties such as surface hardness and wear performance, as can be observed in the present study for Ti6242 alloy.

Figure 6 shows the Kernal average misorientation (KAM) results of the Ti6242 sample before and after the tumble-treatment. (It should be noted that the EBSD maps presented in Figs. 5 and 6 were acquired at different times.) KAM measures the mean angular misorientation between adjacent points within the same grain, serving as a reliable indicator of localized lattice strain and residual stress. In this work, the tumble-finished surface (Fig. 6b) exhibited slightly higher KAM values compared with the untreated counterpart (Fig. 6a). This increase can be associated with the elevated dislocation density generated during tumbling, owing to the repeated and random mechanical impacts imparted to the surface. The corresponding KAM distributions (Fig. 6c) reveal that values infrequently exceed 2.5°, with only a few points in either sample surpassing this limit. The untreated surface presented a lower mean KAM of 0.38°, whereas the tumble-finished layer displayed a slightly higher mean of 0.46°, indicating that the tumbling process induces a modest but measurable increase in lattice distortion.

The tumbling treatment also modified the grain morphology of the α-Ti phase. Figure 7 illustrates the grain shape aspect ratio distribution of the Ti6242 sample in both condition. Before tumble finishing (Fig. 7a, b), the grains exhibited an elongated columnar shape with a low average

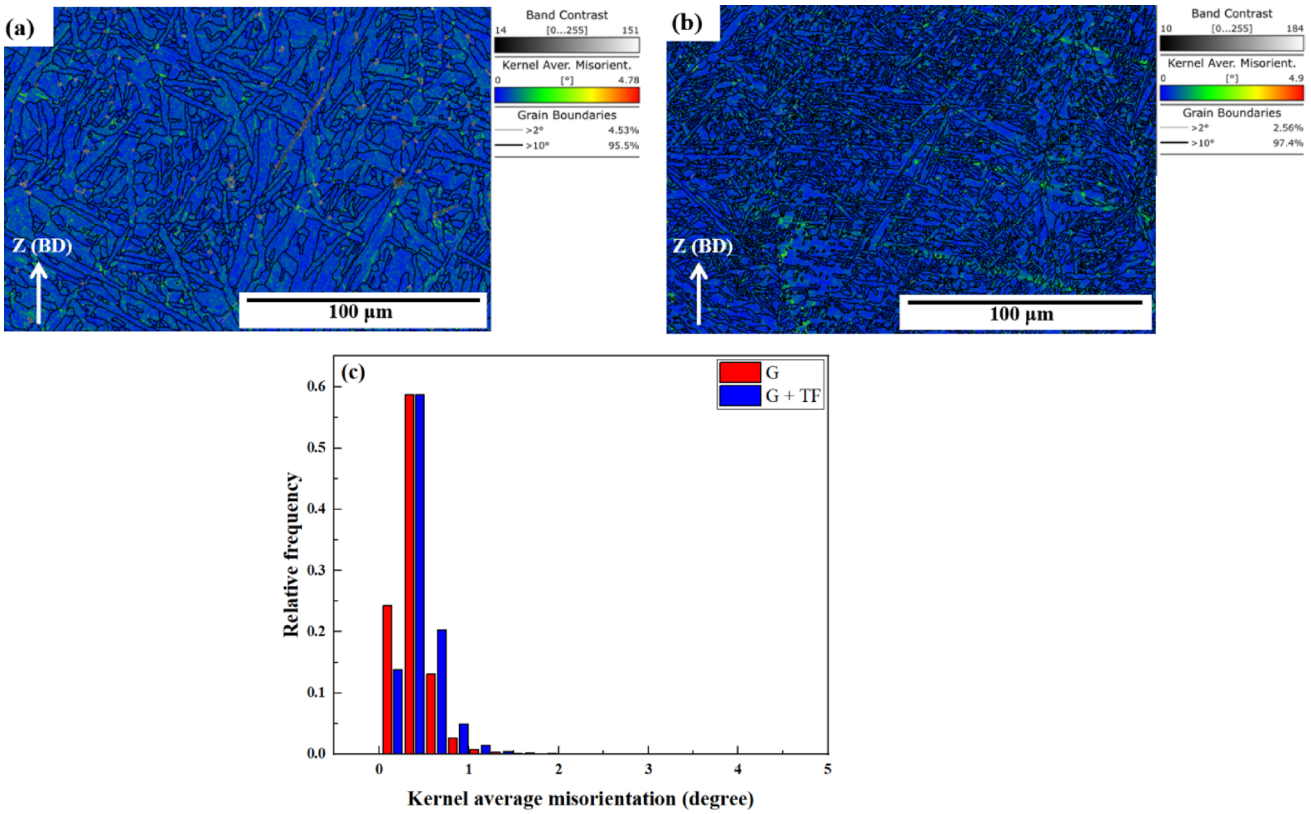


Fig. 6 KAM results for the Ti6242 sample showing **a** cross-section near the upskin, **b** cross-section near the downskin following tumble finishing, and **c** relative frequency vs. KAM without and with tumble finishing

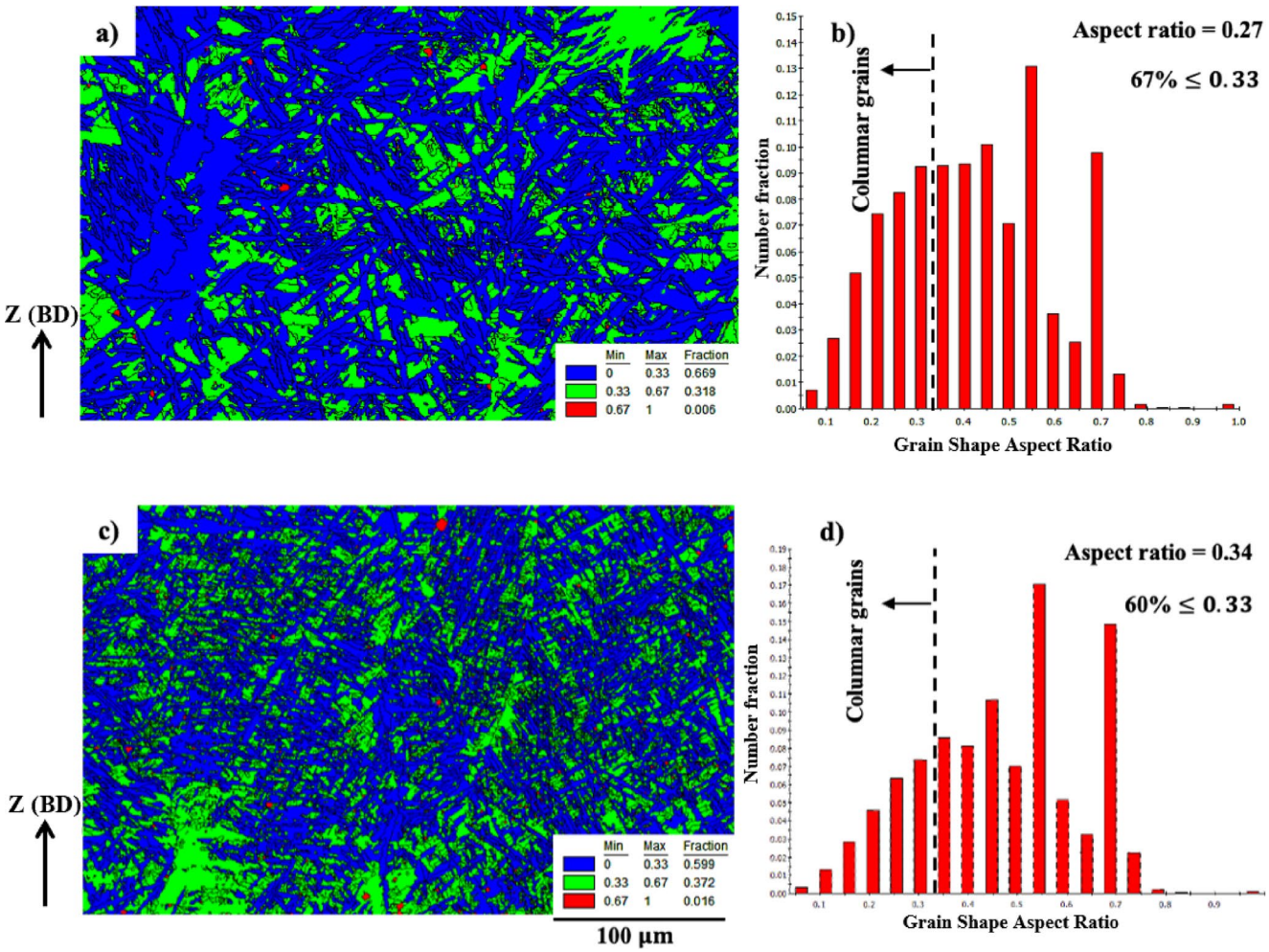


Fig. 7 The grain shape aspect ratio maps and distribution curves of the Ti6242 sample **a**, **b** without, and **c**, **d** with tumble finishing; where blue indicates columnar ($\phi \leq 0.33$), green represents intermediate ($0.33 < \phi \leq 0.67$), and red marks equiaxed grains ($\phi > 0.67$)

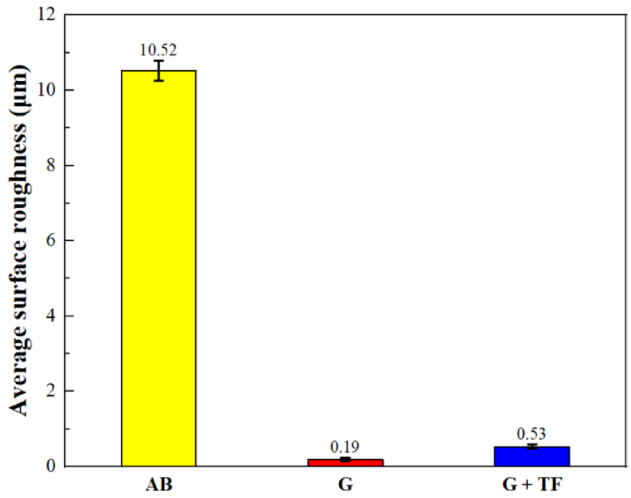


Fig. 8 Average surface roughness (Ra) of AB, G, and G+TF Ti6242 samples

aspect ratio ($\phi \approx 0.27$) and a high fraction of columnar grains (≈67%) aligned along the build direction, reflecting the epitaxial solidification and directional α-plate growth typical of PBF-EB/M Ti6242. After tumbling, the repeated micro-impacts and multidirectional shear stresses at the surface fragmented these columnar grains into smaller and equiaxed subgrains, as shown in Fig. 7c, d. As a result, the average aspect ratio increased to about 0.34 and the fraction of columnar grains decreased to ~60%, indicating a partial transition from elongated to semi-equiaxed morphology.

Figure 8 presents the average surface roughness (*Ra*) of G and G + TF samples. It is revealed that both post-processing routes lead to a substantial enhancement in surface quality compared to the as-built surface after removing the support structure, which exhibits a roughness of ~ 10.5 µm. Among the studied conditions, the G sample shows the lowest roughness, while the G + TF sample presents a slightly higher *Ra* than G. Nevertheless, the application of TF for 2 h following the grinding process still results in a remarkable

reduction in roughness compared to the as-built condition. In addition, G + TF effectively eliminates partially melted powders adhering to the surface and modifies the surface morphology, yielding a significantly smoother overall finish relative to the as-built state. The literature also attests to the efficacy of TF in achieving satisfactory surface quality across a range of AM materials [30, 31]. The findings from the SEM-based surface analysis depicted in Fig. 9 confirm how the selected industrial surface finishing treatments effectively removed the fingerprints of the support structures. As surface roughness diminishes, contact points on the material become more uniform, reducing the likelihood of stress concentrations. In the grinding-only condition, without tumbling, spherical cavity-like pits can still be observed on the surface, whereas after tumbling, the surface appears more uniform.

Figure 10 illustrates a microscopic view of an individual pyramidal particle and its interaction with surface roughness. In this context, (F) represents the contact force, (v) signifies the sliding velocity of the media, and (α) denotes the orientation of media impact. The force (F_n) is responsible for embedding the abrasive particle into the material, while (F_t) facilitates the movement of the abrasive particle in relation to the surface. The abrasive particle may either scratch or displace material laterally, following the flow of the abrasive medium (ploughing), or it may remove material in the form of microchips [41]. Experts have developed numerous studies and analytical models to explore these phenomena in detail [42–45].

The impressive effectiveness of pyramidal media in reducing roughness can be attributed to several factors: specifically, the cutting efficiency of the pyramidal particles, which create smaller contact surfaces with the sample due to their sharp edges (as shown in Fig. 10), resulting in high localized stress and significant material removal [46].

3.2 Mechanical properties

Using the equipment described in this study, attempts were made to perform hardness and wear tests on the as-built (AB) samples; however, due to the high surface roughness and severe irregularities on the surface (Fig. 9a), these tests could not be conducted with acceptable accuracy, and the results were deemed unreliable. In indentation-based tests (such as microhardness or nanoindentation), a fundamental assumption is that the indentation occurs on a nearly flat surface [47]. When the surface roughness is comparable to the indentation depth, this assumption is violated, leading to

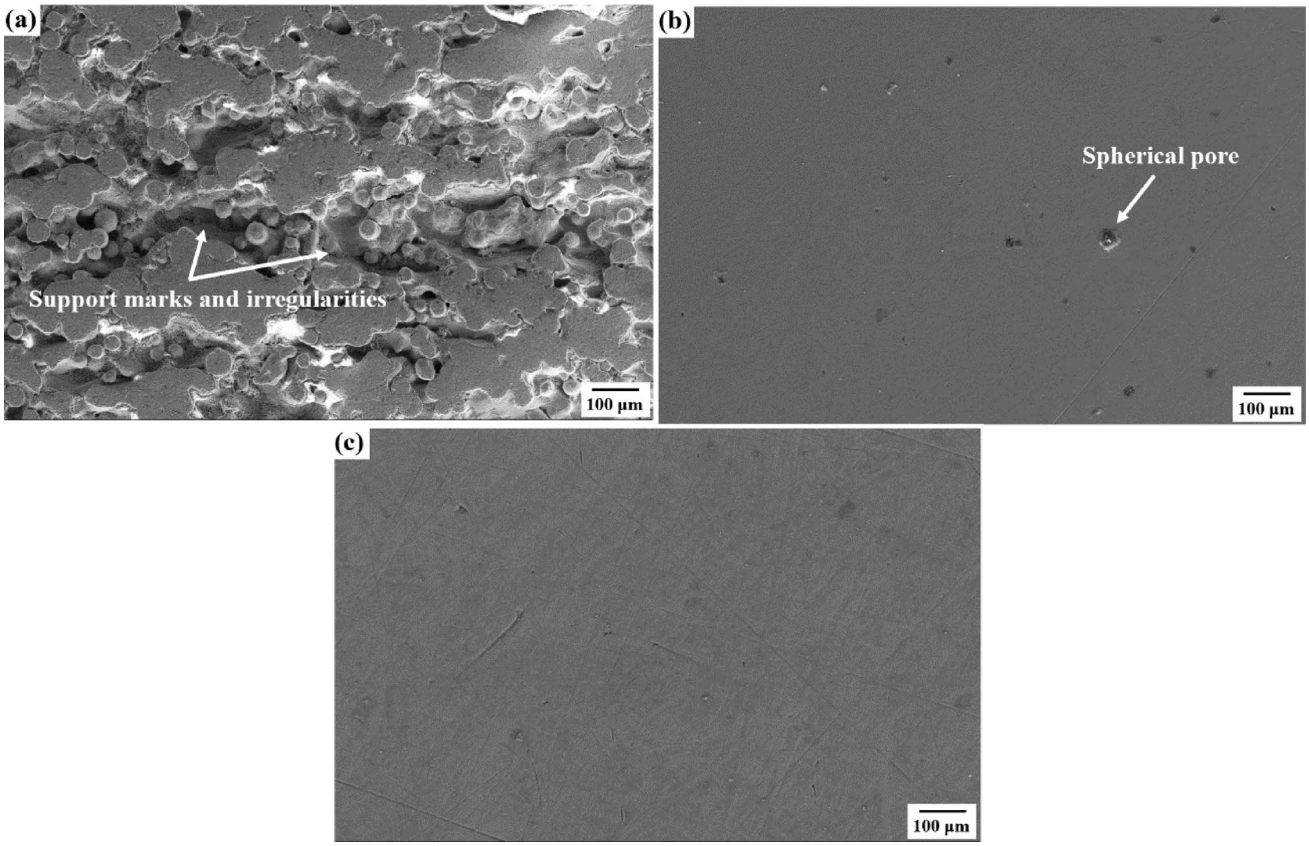


Fig. 9 SEM micrograph of the Ti6242 samples from the downskin plane where the support structures were connected to the sample: **a** AB state and after (**b**) G, and **c** G+TF treatments

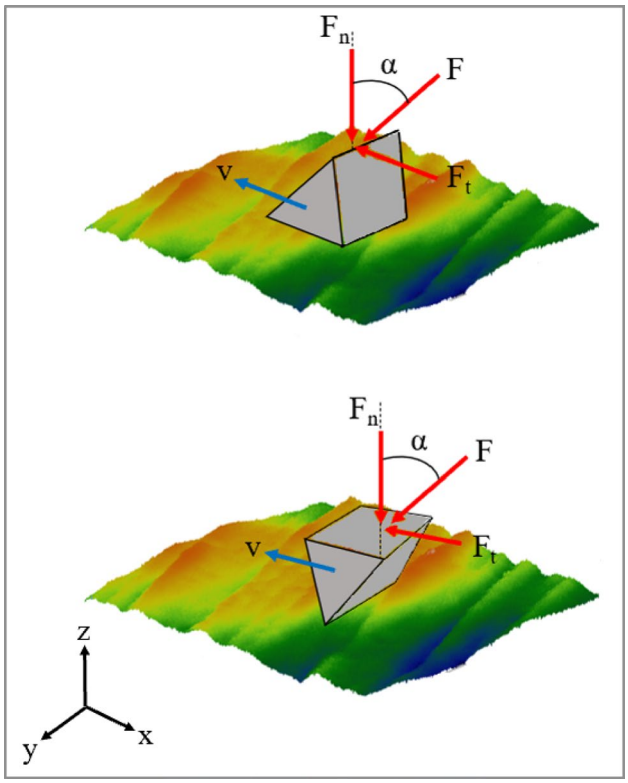


Fig. 10 Schematic illustration of the interaction of the single pyramidal particle with the sample surface

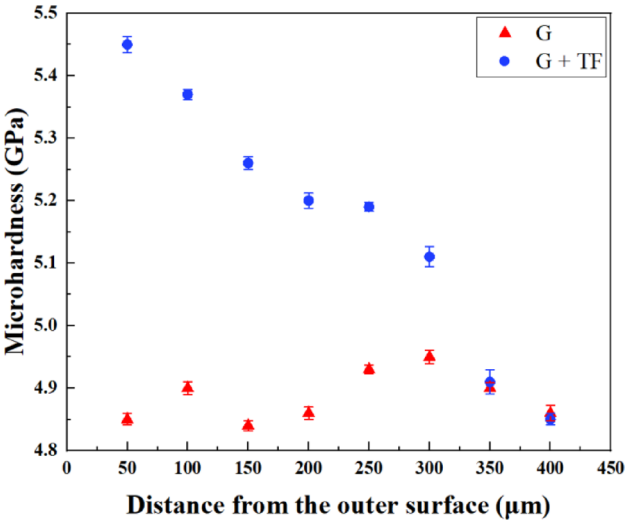


Fig. 11 Microhardness as a function of distance from the outer surface of G and G+TF Ti6242 samples

significant errors in measuring hardness and elastic modulus [48]. Moreover, during indentation on rough surfaces, part of the applied energy is spent flattening the surface asperities rather than deforming the bulk material [49]. This effect leads to high scatter in load–displacement curves and, consequently, poor reproducibility of the measurements.

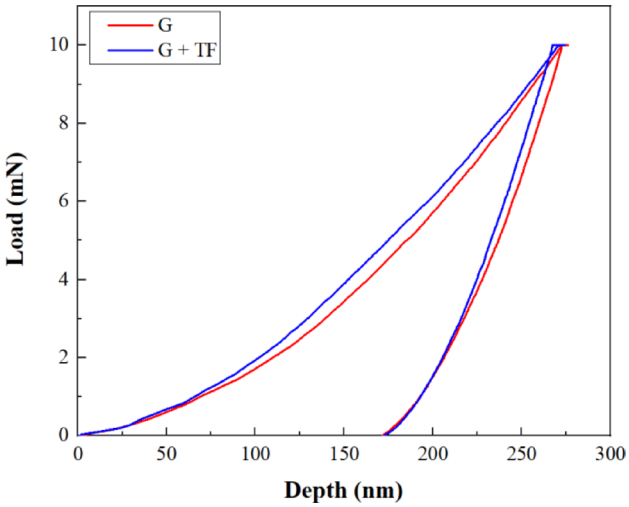


Fig. 12 Indentation loading-unloading plots for Ti6242 alloy after G and G+TF post surface treatments

Similarly, in wear tests, high surface roughness and irregularities alters the real contact conditions, reduces contact uniformity, and changes the mechanisms of friction and material removal. Contact predominantly occurs at the asperities, and as these are progressively worn during the test, the contact area continuously evolves. This phenomenon typically results in large fluctuations in the COF throughout the test, making wear rate and friction measurements highly unreliable.

Based on previous studies on Ti6242 alloy [3, 28], mechanical tests are typically performed on ground surfaces, and the goal of the present study is to compare grind-treated samples with tumble-finished samples.

It is imperative to thoroughly characterize the surface hardness variations following post-processing. The cross-sectional microhardness of Ti6242 alloys is presented in Fig. 11. The average surface and subsurface hardness values for G specimens were determined to be ~ 4.87 GPa. G + TF treatment exhibited a rising trend in the surface hardness of the specimens, with recorded values reaching ~ 5.47 GPa. It is estimated that the G + TF specimens had a harder surface than the ground ones by about 10%. The outcome closely resembled the observations made by Gunessu et al. [26] regarding the impact of tribo-finishing on the surface hardness of Ti6Al4V alloys. The rise in the depth of TF-induced hardness is approximately 350 μm from the outer surface. The elevated hardness can be attributed to the refined grains and an increased dislocation density resulting from the surface's plastic deformation.

Figure 12 shows the characteristic load-displacement profiles obtained through nanoindentation utilizing a maximum load of 10 mN. It is important to note that the high roughness of the as-built samples poses significant challenges in accurately determining elasto-plastic behavior.

Therefore, we focused our analysis on the G and G + TF samples. Further studies utilizing numerical analysis may be advantageous for modeling the mechanical behavior of rough surfaces under load [50, 51].

Evidently, both curves for G and G+TF samples exhibit a comparable parabolic shape during the loading phase, with indentation depth increasing as the load rises, a result of elastic-plastic deformation under the applied force. The indentation depth reaches its zenith at the culmination of the holding stage. Subsequently, a similar linear unloading behaviour is evident in the upper portion of the curves. It is interesting to note that the discrepancy between the curves corresponding to the nano hardness of the samples after G and G+TF was negligible.

The nano hardness values of the examined materials are presented in Table 2. In general, the assessment of nanoindentation hardness depends on the projected area at the final load, typically smaller than the residual projected area employed in microhardness testing, thus resulting in increased hardness values [52]. The nano hardness of the G + TF sample was about 5% higher than the ground one.

Besides the previously mentioned factors contributing to the hardness increase through the TF process, eliminating partially melted irregularities during G + TF can also result in enhanced hardness compared to the G specimens [53]. According to the previous findings, a hard surface can effectively withstand wear. H/E and H^3/E^2 can be used indirectly to study the wear resistance of Ti alloys, as reported in the literature [54, 55]. Materials with higher H/E and H^3/E^2 ratios typically display improved resistance against elastic and plastic deformation [56]. According to the data reported in Table 2, the higher H/E and H^3/E^2 ratios of the G + TF sample are a reliable indicator of good wear resistance for this specimen.

3.3 Friction and wear analysis

Figure 13a–c shows the friction curves of the surfaces connected to the support structure after surface treatments at three testing temperatures. To better illustrate the measurement scatter, the average COF values together with their standard deviations, obtained from three independent tests and calculated over the steady-state region of the friction curves, are presented in Fig. 13d. As presented in Fig. 13a at ambient temperature, there were noticeable fluctuations for the G sample in the COF within the steady-state region of metal-on-metal sliding interactions. These oscillations reduced when the temperature increased to 250 °C and 450 °C. For the G sample at 25 °C, 250 °C and 450 °C and for the G + TF specimens at 250 °C, the COF increased during an initial running-in period and then reached a steady state. This increase can be attributed to the eliminating of surface layers, including oxide films, or environmental contaminants, which weaken the metal-to-metal adhesion between contacting surfaces [57]. Removing these layers leads to increased instances of metal-to-metal and/or metal-to-wear particle contact, elevating the adhesive and ploughing elements of the COF. Once the surface layers were entirely eradicated and a balance was achieved between wear debris generation and expulsion, the COF stabilized at a constant value of around 0.5.

Table 2 Nanohardness and elastic modulus of the Ti6242 specimen after G and G+TF post treatments

Post-treatment	Nano-hardness (GPa)	Elastic modulus (GPa)	H/E	H^3/E^2
G	7.42±0.03	154.65±3.21	0.0479	0.0170
G+TF	7.83±0.02	160.17±4.39	0.0488	0.0187

For the G + TF sample at 25 °C (Fig. 13a), the COF starts from 0.25 and continues to about 0.39, which is lower than the COF of G sample at room temperature (around 0.52). In fact, the TF layer in this sample has been preserved throughout the wear path and has reduced the COF by approximately 25%. The reduced and stabilized COF might be attributed to grain refinement and compressive residual stress imposition through TF treatment [58]. This process induces strain hardening in the surface layer, leading to diminished surface irregularities [59]. Consequently, higher micro-hardness is another crucial factor contributing to the reduction of COF. It should be noted that the relatively higher roughness of the G + TF specimen compared to the G sample (Fig. 8) did not have a detrimental effect on the tribological behaviour.

The observed shifts in COF at 250 °C suggest that the tribological effectiveness of the TF-induced surface condition is significantly reduced at this temperature. Meanwhile, at 450 °C, the overall COF is lower than at 250 °C. In the case of the G + TF sample at 450 °C, the COF witnesses an ascent from 0.2 to 0.3 within 500 s, culminating in a sudden upswing to 0.4. This transition indicates that the beneficial influence of the TF-modified near-surface region progressively diminishes during sliding. Tribological transitions manifest as alterations in frictional forces throughout sliding, primarily driven by evolving surface conditions. It's noteworthy that material hardness diminishes notably at elevated temperatures, with this effect being more pronounced in Al_2O_3 balls compared to the titanium samples [4], thereby influencing the tribological behaviour of the system. In our studied system, the COF has been diminished under the temperature of 450 °C, which can be attributed to the significant reduction in the hardness of alumina, making the softer alumina ball less efficient in removing material from the sliding contact surface. On the other hand, the debris and surface oxides are affected by increasing temperature. At higher temperatures, oxygen-rich oxide debris layers can

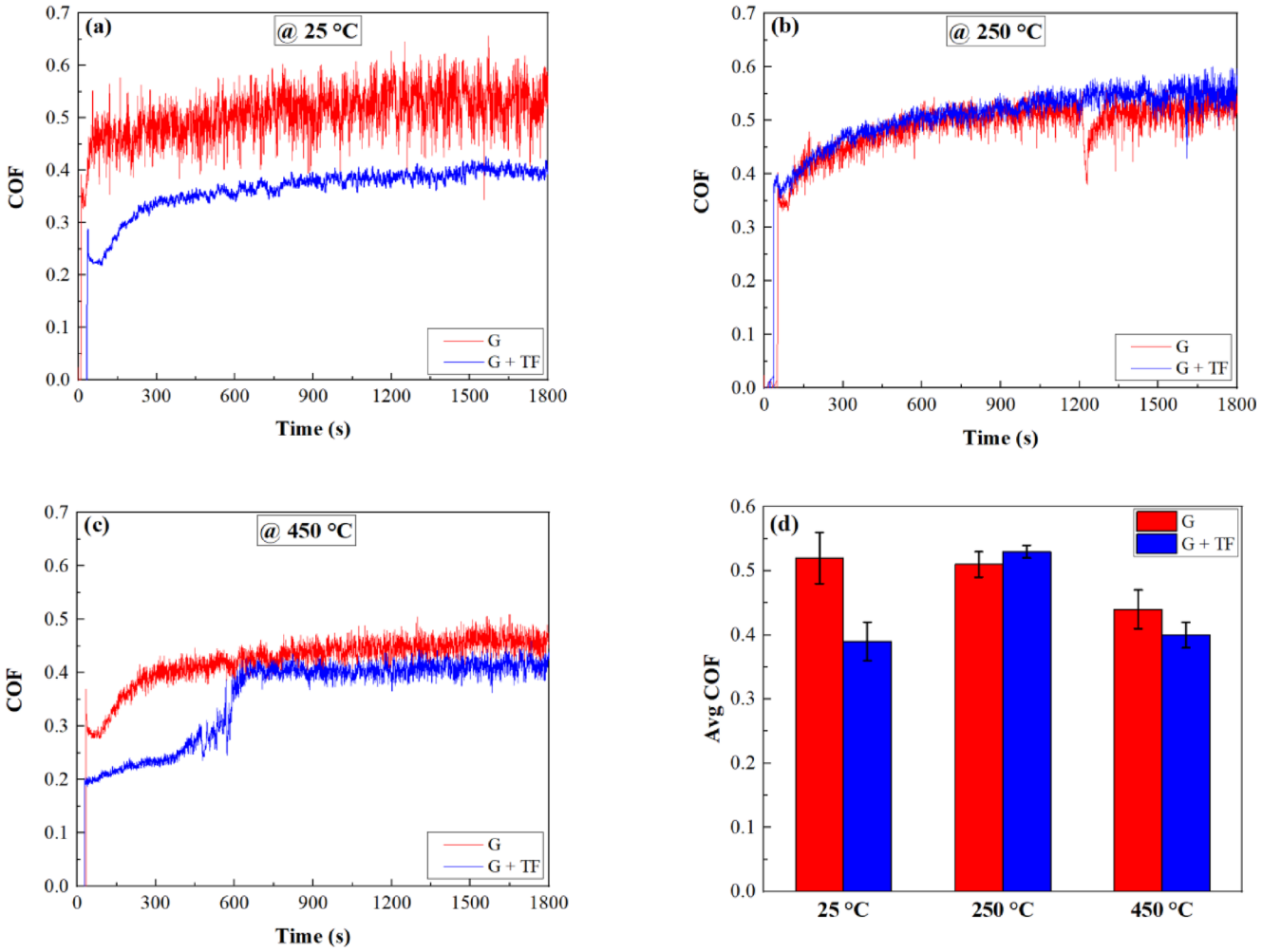


Fig. 13 The friction curves of Ti6242 sample after G and G+TF post treatments at **a** 25 °C, **b** 250 °C and **c** 450 °C. **d** Average COF for the different temperatures

provide a more wear-resistant protective layer [60]. Jia et al. [61] found that with increasing temperature, titanium alloys tend to form compact oxide layers mainly composed of TiO_2 and Al_2O_3. These oxides act as a protective tribo-film, reducing direct metal-to-metal contact and thereby improving wear resistance. Importantly, this explains the non-monotonic variation of the average COF for the G + TF sample: it rises to a maximum at 250 °C because the strengthening and residual-stress effects induced by TF become less effective under these intermediate thermal conditions, promoting increased metal-to-metal interaction, while at 450 °C, the formation of a compact, oxygen-rich oxide tribofilm and the softened alumina counterbody reduce adhesive and ploughing contributions, resulting in a lower COF.

The microstructure of titanium alloys, including Ti6242, plays a significant role in influencing wear behavior. Studies on similar titanium alloys, such as TC21 and Ti6Al4V, have demonstrated that basketweave and lamellar microstructures provide better wear resistance compared to single-phase structures [62–64]. This improved wear resistance is largely due to the presence of β/α interfaces and dispersed α precipitates [62]. Hence, the tribological performance observed in this study can also be related to the inherent microstructural characteristics of Ti6242 and their evolution during surface treatments and testing temperatures.

The wear depth profiles and wear volume of the Ti6242 samples after the wear tests are presented in Fig. 14. The volume loss ($V = 2\pi rS$) was calculated according to Ref [57], where r represents the radius of the wear track (10 mm) and S is the cross-sectional area of the wear depth profiles, determined using OriginPro 2025 software. For each sample, S was obtained as the average value of three independent wear track profiles measured at different positions along the sliding path. The results indicate that the G + TF sample exhibited the lowest wear volume at room temperature, whereas the G sample showed the highest material loss under the same conditions. This behavior is consistent with the frictional response of the samples. G sample at 25 °C

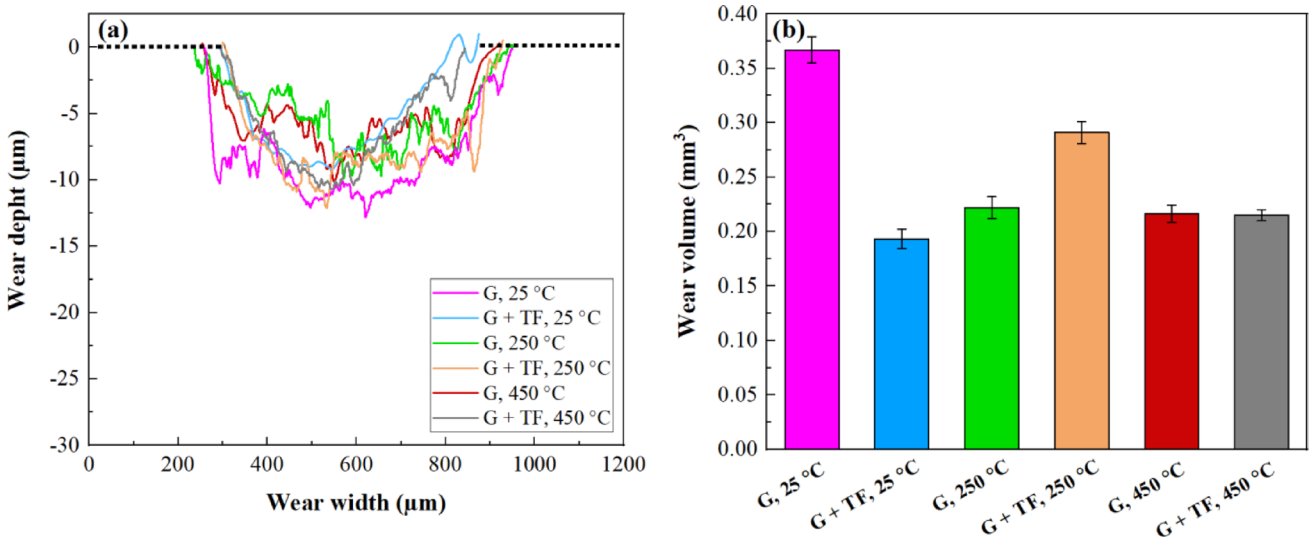


Fig. 14 Wear depth profiles and wear volumes of the Ti6242 samples

with the highest wear volume displayed pronounced fluctuations in the COF during the sliding process, suggesting a less stable tribological behavior and more severe wear.

As shown in Fig. 13, the effectiveness of the modified surface layer was reduced under all conditions except for the G+TF sample at 25 °C, where a more sustained protective behavior was observed. To get more information on the wear mechanisms, the worn surface of the samples was examined by SEM in detail, and the results are presented in Fig. 15. The sliding direction is shown by blue arrows. Also, EDS analysis was performed on the worn surfaces, and the results are reported in Table 3. As presented in Fig. 15a, the worn surface of the G+TF specimen at room temperature was almost smooth and characterized by a few spalling pits and wear debris. Moreover, EDS analysis showed a high percentage of Ti element, around 96%.

Regarding the other conditions, the SEM images of the worn surfaces are almost identical (Fig. 15b–f). The most prominent feature is the presence of numerous furrows, indicating the formation of channels or grooves across the surface. These furrows are likely a result of the ploughing action, which is evident through the presence of ploughing lines that crisscross the surface. As a result, the presence of abrasive wear is noticeable. Similar ploughing-dominated wear mechanisms have also been reported for Ti-based alloys under dry sliding conditions [65, 66].

The SEM observations also indicate that the G samples exhibit more pronounced scratches and grooves, generating higher amounts of wear debris. In contrast, the G + TF sample, despite having slightly higher Ra, features microvalleys and recesses that can trap wear debris, preventing it from contributing to third-body abrasion and thereby mitigating additional surface damage. This debris-trapping effect, together with surface hardening and the presence of residual compressive stress from the TF treatment, likely contributes to the improved tribological performance of the G + TF sample. Moreover, in a previously published study by the first author [67], the role of surface textures and micro-cavities in enhancing tribological and mechanical properties, even in surfaces with slightly higher roughness, was demonstrated. Similar effects have also been reported in the literature [68, 69].

Additionally, the SEM image depicts signs of spalling, where localized fragments of material have broken away from the surface. Moreover, the worn surface exhibits an array of wear debris, indicating that material removal and three-body abrasives have occurred. According to Table 3, the G sample at 25 °C is associated with a high percentage of nearly 10% of the Al element, indicating adhesive wear between the Al_2O_3 ball and the surface of the Ti alloy. The result is consistent with high fluctuations in the friction diagram (Fig. 13a). It is also important to consider the role of real contact area in this behavior. Although the G surface exhibits lower *Ra*, extremely smooth metallic surfaces can promote a larger real contact area under dry sliding conditions, thereby increasing the probability of forming strong adhesive junctions (micro cold-welding) with the counterbody and leading to pronounced COF fluctuations. In contrast, the slightly higher roughness and textured morphology of the G + TF surface reduce the continuity of real contact, limiting the formation of large adhesive junctions and stabilizing the friction response [70].

A similar adhesive mechanism was reported by Woźniak et al. [71], who investigated the tribological behavior of a Ti-based alloy against an Al_2O_3 ball under both dry and lubricated conditions at room temperature. They observed that, in the absence of surface modification, the worn surfaces showed distinct adhesion marks and transfer layers.

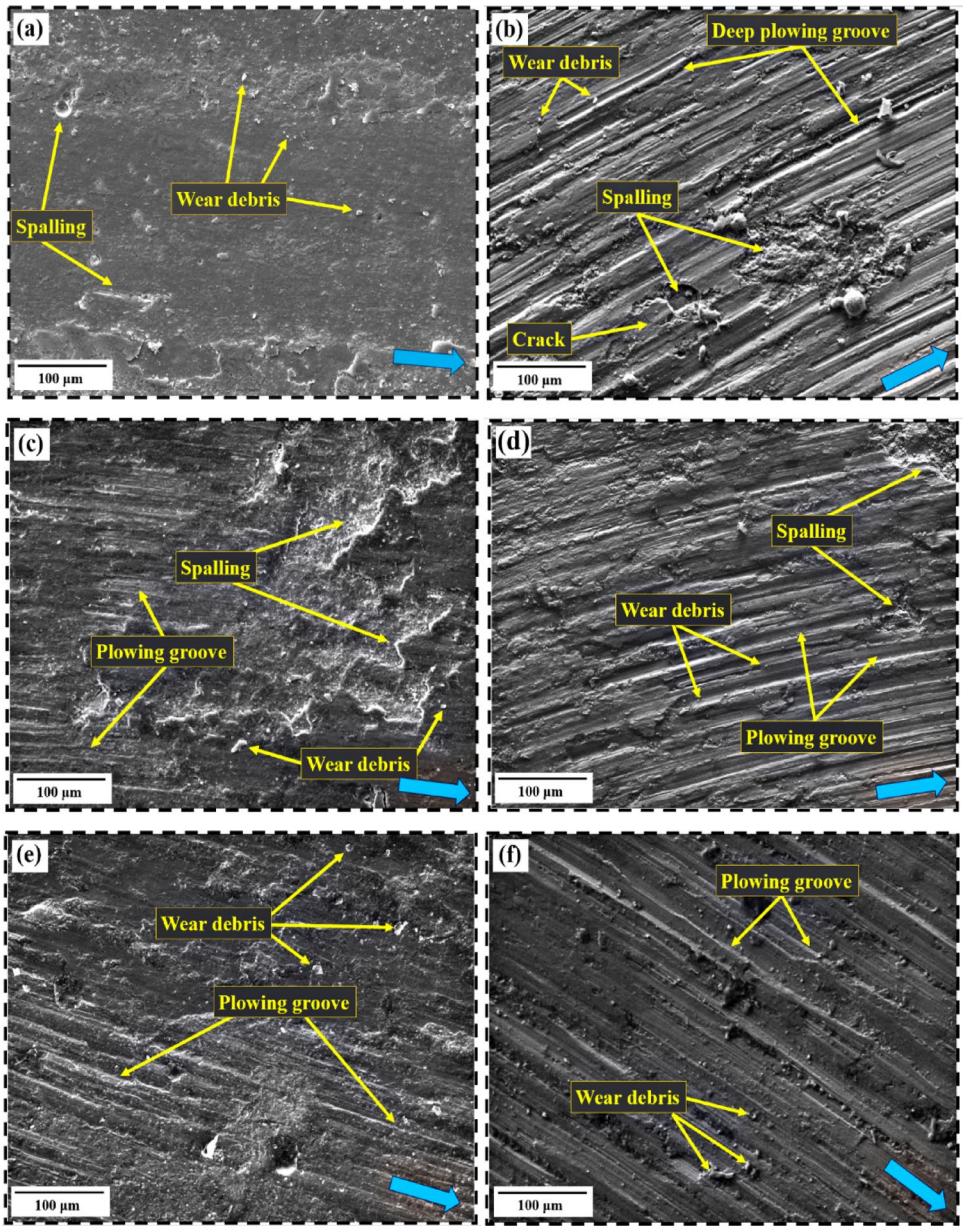


Fig. 15 SEM images of wear surfaces of Ti6242 sample after G+TF treatment at **a** 25 °C, **c** 250 °C and **e** 450 °C, and after G treatment at **b** 25 °C, **d** 250 °C and **f** 450 °C (All wear tests were performed on the x–y planes)

Table 3 EDS analysis results on the worn surfaces (black dashed lines) depicted in Fig. 15

	Element (wt%)						
	Ti	O	Al	Si	Zr	Mo	Sn
Figure 15a	96.45	1.28	0.65	0.53	0.51	0.31	0.27
Figure 15b	85.21	3.69	9.42	0.62	0.53	0.28	0.25
Figure 15c	68.25	25.69	4.70	0.50	0.46	0.21	0.19
Figure 15d	65.42	27.37	5.81	0.48	0.45	0.30	0.17
Figure 15e	56.91	36.83	4.37	0.62	0.60	0.39	0.28
Figure 15f	57.71	33.72	6.85	0.57	0.52	0.33	0.30

This adhesive interaction between the titanium oxide layer and the alumina counterbody is attributed to the high chemical affinity and comparable hardness of TiO_2 and Al_2O_3, which promotes localized bonding and subsequent material transfer during sliding. As expected, the degree of surface damage at 450 °C is less than 250 °C. Both specimens, at 250 °C, show the presence of oxygen element with a percentage higher than 25, confirming surface oxidation and oxidative wear. The same situation was observed for the

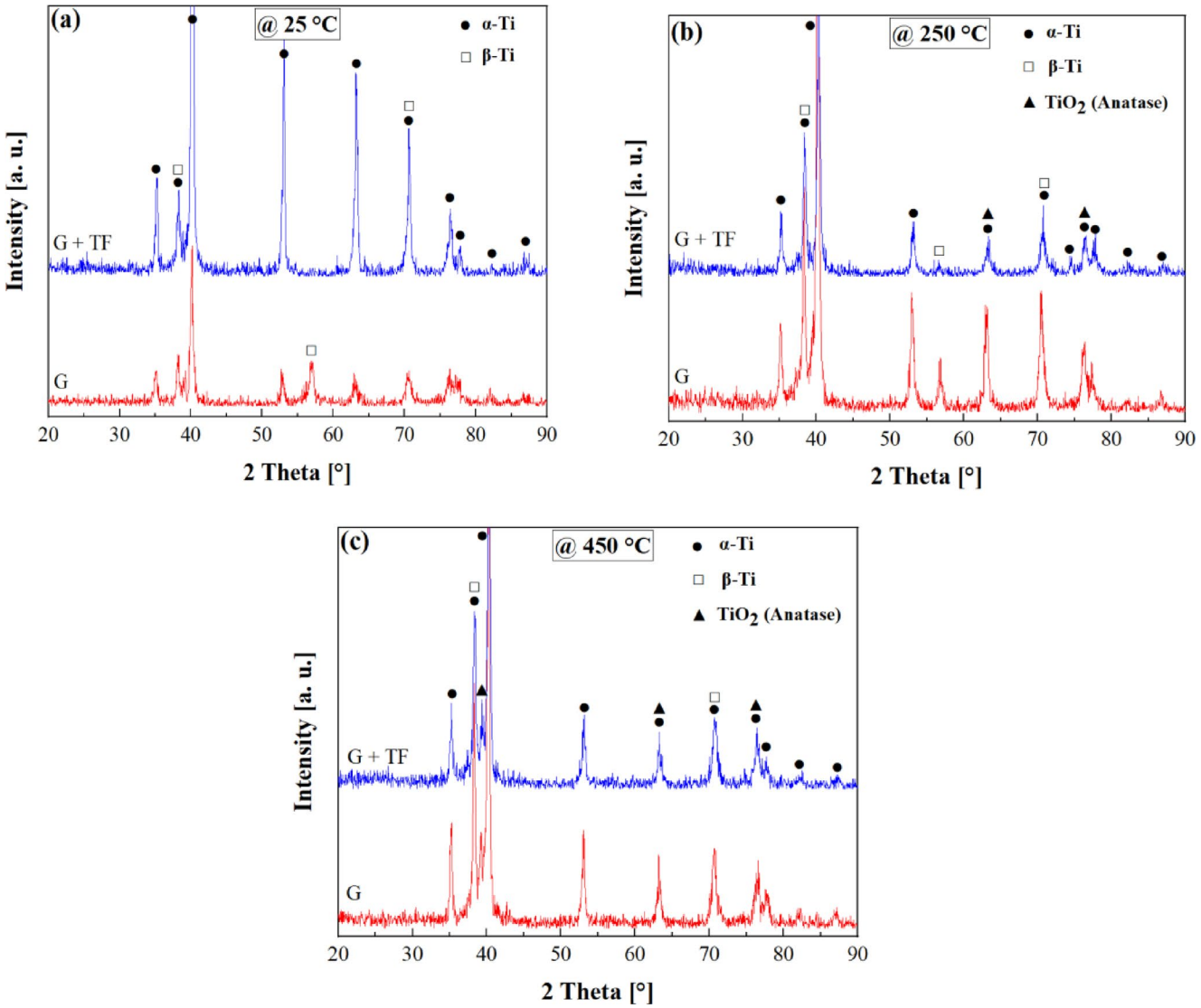


Fig. 16 The XRD patterns of the Ti6242 sample after G and G + TF post treatments at **a** 25 °C, **b** 250 °C and **c** 450 °C

samples at higher temperatures but with higher oxygen concentration and, consequently, more surface oxidation.

In order to understand better the formed phases, the XRD analysis was conducted on the surfaces of G and G + TF samples at different temperatures, and their patterns are illustrated in Fig. 16. As can be seen, the main detected phases were α, with some traces of β phase detected, identified by relatively weak peaks. While the α phases in titanium alloys are relatively softer than those in iron and steel materials, their hardness still surpasses that of the β phase [7]. As observed in Fig. 16a, the G sample exhibits an additional peak at room temperature corresponding to the β phase, which possesses lower hardness. Consequently, this can reduce wear resistance, particularly when compared to the G + TF sample. In fact, the softness of the β phase helps to remove it during the TF process of titanium alloy. Furthermore, the G + TF specimen shows more intense and stronger peaks of α, indicating the higher hardness and strength. It is well-known that a harder surface is more resistant to the formation of wear debris and microcracks during sliding contact, reducing material loss and improving tribological performance. The G + TF treatment enhances surface hardness by increasing the dislocation density and refining the grain structure, both of which are essential for improving the alloy's wear resistance during high-temperature and high-load applications. Recent studies have confirmed that tumble finishing can substantially reduce surface roughness while inducing near-surface hardening and compressive residual stresses, contributing to improved fatigue and wear resistance of metallic alloys [29]. Rotary barrel tumbling has also been shown to promote a more homogeneous microstructure and a significant reduction in R_a, up to 70%

in high-carbon steels, while ensuring consistent mechanical response across multiple sample [72]. Similarly, vibratory tumbling combined with thermal treatment enhanced the surface hardness of additively manufactured stainless steels by 15–20%, correlating directly with higher wear resistance [73]. These findings collectively confirm that the improvement of near-surface microstructure through controlled tumbling processes is a key factor in achieving superior tribological performance.

Regarding the temperatures of 250 °C and 450 °C (Fig. 16a, b), the XRD patterns were identical for both samples. Except for the α and β phases, the TiO_2 (anatase) phase was also detected at high temperatures, with the difference that at a temperature of 450 °C, an extra peak of anatase was formed at $2\theta = 39.164°$. During sliding, the oxide layer formed by the reaction of titanium and oxygen shows two opposite effects. On one hand, the weak adhesion between the oxide layer and the surface leads to its breakdown, reducing wear resistance. On the other hand, at high temperatures, the oxide layer acts as a solid lubricant, helping to lower friction. Titanium oxide films are known to reduce adhesive wear by forming a protective layer that prevents direct metal-to-metal contact, improving wear resistance at elevated temperatures [74]. The improvement in COF at 450 °C compared to 250 °C can be attributed to the more TiO_2 formation and its self-lubrication properties. Formation of anatase TiO_2 upon temperatures of 200 °C, with a highly crystalline form appearing after 400 °C, is also reported in the work by Fagan et al. [75].

It should be noted that at 250 °C, the overall frictional behavior of the G and G + TF samples is largely comparable. This observation is consistent with the limited tribological efficiency of the TF-induced surface condition at this temperature. Regarding oxide formation, at 250 °C the TiO_2 layer is relatively thin and mechanically unstable. Its weak adhesion to the substrate promotes repeated formation–fracture cycles, which does not provide sustained lubrication. In contrast, at 450 °C, the higher oxygen diffusion and increased anatase peak intensity in XRD indicate the formation of a more continuous and compact oxide tribofilm [75]. This stable oxide layer acts as a protective solid lubricant, reducing direct metal-to-metal contact and lowering the COF. Although the measured wear depths (10–15 μm) remain well within the ~ 350 μm hardened subsurface layer induced by TF, the limited stability and lubricating capability of the oxide layer at 250 °C appears to be the dominant factor governing the tribological response at this temperature.

4 Conclusions

In this study, Ti6242 alloys were produced using the PBF-EB/M process. The mechanical and wear properties of the ground surfaces connected to the support structure were assessed and compared with those subjected to hybrid grinding and tumble finishing treatment. The key findings can be drawn as follows:

- Ti6242 alloy exhibited a typical basketweave α+β microstructure. During tumble finishing processes, mechanical deformations on the specimen's surface significantly increased dislocation density.
- EBSD analysis showed that tumbling induced grain subdivision and partial transition to semi-equiaxed morphology. The higher KAM values and reduced texture intensity indicated increased dislocation density and lattice distortion near the surface.
- Although the roughness of the tumble-finished samples was slightly greater than that of the ground ones, the tumble finishing technique generated a much better surface than the as-built sample, while also demonstrating superior tribological performance compared to the ground condition, making it a promising candidate for achieving high surface quality in AM parts with complex shapes.
- Since grinding-tumble finishing alters the surface and subsurface microstructure of the manufactured specimens, it resulted in an approximately 10% increase in the hardness when compared to ground specimens.
- The influence of tumble finishing on the COF of Ti6242 at room temperature was considerable (around 25% reduction of COF compared to ground specimens). In this case, the surface of the worn track was associated with minor damage.
- With increasing temperature or transfer from tumble finishing treatment to grinding, large spalling, ploughing lines and abrasive-oxidative wear were observed on the surface. On the other hand, when the temperature increased to 450 °C, the formation of higher titanium oxide, with its inherent lubricating properties, resulted in lower COF values compared to those at 250 °C.

All in all, it can be concluded that the combined application of grinding and tumble finishing has proven to be an effective strategy for enhancing the surface quality and tribological performance of Ti6242 components produced via PBF-EB/M. This approach offered a rapid and cost-effective solution for eliminating surface imperfections, such as porosity and roughness, associated with the PBF-EB/M process. The resulting improvement in surface finish lead

to enhanced wear resistance and reduced friction, making these components suitable for demanding applications.

Author contributions Farideh Davoodi: Methodology, Formal analysis, Investigation, Visualization, Writing—Original Draft., Parisa Moazzen: Specimen preparation, data acquisition, measurements, Visualization, Writing., Mohammad Taghian: Methodology, Formal analysis, Investigation, Writing., Manuela Galati: Production of all Sample, Writing—Review and Editing., Mohsen Mohammadi: Supervision, Review and Editing., Abdollah Saboori: Conceptualization, Supervision, Production of all Sample, Validation, Project administration, Resources, Writing—Review and Editing.

Funding Open access funding provided by Politecnico di Torino within the CRUI-CARE Agreement.

Data availability No datasets were generated or analysed during the current study.

Declarations

Conflict of interest The authors declare no financial or commercial conflict of interest.

Open Access This article is licensed under a Creative Commons Attribution 4.0 International License, which permits use, sharing, adaptation, distribution and reproduction in any medium or format, as long as you give appropriate credit to the original author(s) and the source, provide a link to the Creative Commons licence, and indicate if changes were made. The images or other third party material in this article are included in the article's Creative Commons licence, unless indicated otherwise in a credit line to the material. If material is not included in the article's Creative Commons licence and your intended use is not permitted by statutory regulation or exceeds the permitted use, you will need to obtain permission directly from the copyright holder. To view a copy of this licence, visit http://creativecommons.org/licenses/by/4.0/.

References

1. Ballat-Durand D, Bouvier S, Risbet M, Pantleon W (2019) Through analysis of the microstructure changes during linear friction welding of the near-α titanium alloy Ti-6Al-2Sn-4Zr-2Mo (Ti6242) towards microstructure optimization. Mater Charact 151:38–52
2. Han J-Y, Kim J-H, Cho Y-H, Kwon YS, Park JH, Kim K-S et al (2025) Microstructure and tensile deformation mechanism of Ti–6Al–2Sn–4Zr–2Mo alloy fabricated by directed energy deposition process. J Mater Res Technol 38:533
3. Saboori A, Tognoli E, Galati M, Denti L (2025) Electron beam powder bed fusion of Ti–6Al–2Sn–4Zr–2Mo alloy: microstructure evolution and high-temperature mechanical properties. Progr Additive Manuf 10:6627–6641
4. Heilig S, Ramezani M, Neitzert T, Liewald M (2018) Tribological performance of duplex-annealed Ti-6Al-2Sn-4Zr-2Mo titanium alloy at elevated temperatures under Dry sliding condition. J Mater Eng Perform 27:2003–2009
5. Chamanfar A, Pasang T, Ventura A, Misiolek W (2016) Mechanical properties and microstructure of laser welded Ti–6Al–2Sn–4Zr–2Mo (Ti6242) titanium alloy. Mater Sci Eng A 663:213–224
6. Galati M, Defanti S, Saboori A, Rizza G, Tognoli E, Vincenzi N et al (2022) An investigation on the processing conditions of Ti-6Al-2Sn-4Zr-2Mo by electron beam powder bed fusion: microstructure, defect distribution, mechanical properties and dimensional accuracy. Addit Manuf 50:102564
7. Ju J, Zhou Y, Wang K, Liu Y, Li J, Kang M, Wang J (2020) Tribological investigation of additive manufacturing medical Ti6Al4V alloys against Al_2O_3 ceramic balls in artificial saliva. J Mech Behav Biomed Mater 104:103602
8. Lin Z, Song K, Yu X (2021) A review on wire and arc additive manufacturing of titanium alloy. J Manuf Process 70:24–45
9. Mosallanejad MH, Abdi A, Karpasand F, Nassiri N, Iuliano L, Saboori A (2023) Additive manufacturing of titanium alloys: processability, properties, and applications. Adv Eng Mater 25:2301122
10. Mosallanejad MH, Ghanavati R, Behjat A, Taghian M, Saboori A, Iuliano L (2024) Untapped opportunities in additive manufacturing with metals: from new and graded materials to post-processing. Metals 14:425
11. Praveenkumar K, Vishnu J, Gopal V, Arivarasu M, Lackner JM, Meier B et al (2024) High temperature dry sliding wear behaviour of selective laser melted Ti-6Al-4V alloy surfaces. J Mater Process Technol 329:118439
12. Cui Y, Aoyagi K, Koizumi Y, Fujieda T, Chiba A (2020) Enhanced oxidation resistance of a titanium–based alloy by the addition of boron and the application of electron beam melting. Addit Manuf 31:100971
13. Algardh JK, Horn T, West H, Aman R, Snis A, Engqvist H et al (2016) Thickness dependency of mechanical properties for thin-walled titanium parts manufactured by Electron Beam Melting (EBM)®. Additive Manuf 12:45–50
14. Yu G, Chao C, Wang Q-B, Min L, Cao Y-K, Pan Y-M, Tan L-M (2022) Effect of porosity on mechanical properties of porous tantalum scaffolds produced by electron beam powder bed fusion. Trans Nonferr Met Soc China 32:2922–2934
15. Aziziderouei M, Chen Z, Pasang T, Newby M, Tao Y (2020) Effect of lack of fusion formed during electron beam powder bed fusion of Ti-6Al-4V alloy on impact toughness. J Mater Eng Perform 29:4978–4990
16. Manco E, Scherillo F, Franchitti S, Borrelli R (2024) Improving surface quality and fatigue life of electron beam melted Ti6Al4V by chemical machining. J Mater Eng Perform 33:2552–2561
17. Davoodi F, Taghian M, Carbone G, Saboori A, Iuliano L (2023) An overview of the latest progress in internal surface finishing of the additively manufactured metallic components. Materials 16:3867
18. Ma C, Andani MT, Qin H, Moghaddam NS, Ibrahim H, Jahadakbar A et al (2017) Improving surface finish and wear resistance of additive manufactured nickel-titanium by ultrasonic nano-crystal surface modification. J Mater Process Technol 249:433–440
19. Liang X, Du P, Li S, Zhang C (2022) Tribological properties of additive manufactured Ti6Al4V against cemented carbide under dry sliding conditions. Tribol Int 167:107358
20. Lizzul L, Bertolini R, Ghiotti A, Bruschi S (2021) Turning of additively manufactured Ti6Al4V: effect of the highly oriented microstructure on the surface integrity. Materials 14:2842
21. Lesyk D, Dzhemelinskyi V, Martinez S, Mordyuk B, Lamikiz A (2021) Surface shot peening post-processing of inconel 718 alloy parts printed by laser powder bed fusion additive manufacturing. J Mater Eng Perform 30:6982–6995
22. Barone S, Neri P, Orsi S, Paoli A, Razionale AV, Tamburrino F (2019) Properties enhancement of carbon PA 3D-printed parts by post-processing coating-based treatments. In: Design tools and methods in industrial engineering: proceedings of the international conference on design tools and methods in industrial engineering,

ADM 2019, September 9–10, Modena, Italy: Springer; 2020. 837–847
23. Iquebal AS, El Amri S, Shrestha S, Wang Z, Manogharan GP, Bukkapatnam S (2017) Longitudinal milling and fine abrasive finishing operations to improve surface integrity of metal AM components. Proc Manuf 10:990–996
24. Maleki E, Bagherifard S, Unal O, Sabouri F, Bandini M, Guagliano M (2022) Effects of different mechanical and chemical surface post-treatments on mechanical and surface properties of as-built laser powder bed fusion AlSi10Mg. Surf Coat Technol 439:128391
25. Calignano F, Mercurio V, Rizza G, Galati M (2022) Investigation of surface shot blasting of AlSi10Mg and Ti6Al4V components produced by powder bed fusion technologies. Precis Eng 78:79–89
26. Güneşsu E, Yılmaz MS, Taşçıoğlu E, Sharif S, Kaynak Y (2022) Effect of drag finish post-processing on surface integrity and wear behavior of Ti-6Al-4V fabricated by laser powder bed fusion additive manufacturing. J Mater Eng Perform 31:9962–9971
27. Zeng Q, Sun S, Pang Z, Wei X (2024) Study on high-temperature, ultra-low wear behaviors of Ti6Al4V alloy with thermal oxidation treatment. Coatings 14:416
28. Naghyan Fesharaki M, Atapour M, Nahvi SM, Galati M, Saboori A (2025) Tribological response and microstructure evolution of electron beam powder bed fusion additively manufactured Ti–6Al–2Sn–4Zr–2Mo alloy. Progr Addit Manuf 663:1–16
29. Maleki E, Bagherifard S, Unal O, Revuru M, Bandini M, Guagliano M (2023) The efficiency of tumble finishing as a final post-treatment for fatigue enhancement of notched laser powder bed fusion AlSi10Mg. Sci Rep 13:4602
30. Benedetti M, Torresani E, Leoni M, Fontanari V, Bandini M, Pederzolli C, Potrich C (2017) The effect of post-sintering treatments on the fatigue and biological behavior of Ti-6Al-4V ELI parts made by selective laser melting. J Mech Behav Biomed Mater 71:295–306
31. Denti L, Bassoli E, Gatto A, Santecchia E, Mengucci P (2019) Fatigue life and microstructure of additive manufactured Ti6Al4V after different finishing processes. Mater Sci Eng A 755:1–9
32. Maleki E, Bagherifard S, Bandini M, Guagliano M (2021) Surface post-treatments for metal additive manufacturing: progress, challenges, and opportunities. Addit Manuf 37:101619
33. Xiao Z, Zhou J, Qi Y, Huang Y, Chen S, Wang J, Zhu H (2023) The effect of support structure on residual stress in laser powder bed fusion of Ti6Al4V alloy. J Mater Res Technol 27:7927–7934
34. Aniołek K, Barylski A, Kowalewski P, Kaptacz S (2022) Investigation of dry sliding friction, wear and mechanical behavior of the Ti-6Al-7Nb alloy after thermal oxidation. Materials 15:3168
35. Sousa L, Antunes RD, Fernandes JC, Alves AC, Toptan F (2023) Influence of Al_2O_3 reinforcements and Ti-Al intermetallics on corrosion and tribocorrosion behavior of titanium. Surf Coat Technol 470:129835
36. Zhang Z, Li X, Almandoz E, Fuentes GG, Dong H (2017) Sliding friction and wear behaviour of Titanium-Zirconium-Molybdenum (TZM) alloy against Al_2O_3 and Si3N4 balls under several environments and temperatures. Tribol Int 110:348–357
37. Munagala VNV, Bessette S, Gauvin R, Chromik RR (2020) Sliding wear of cold sprayed Ti6Al4V coatings: Effect of porosity and normal load. Wear 450:203268
38. Davoodi F, Ashrafizadeh F, Atapour M, Rikhtehgaran R (2022) A novel approach for evaluation of load bearing capacity of duplex coatings on aluminum alloy using PLS and SVR models. Trans Nonferrous Met Soc China 32:1834–1851
39. Davoodi F, Varmaziar S, Atapour M, Iuliano L, Saboori A (2025) In vitro corrosion and bio-tribocorrosion performance of electron beam powder bed fusion Ti6Al4V specimens with lapping and superfinishing treatments. Progr Addit Manuf 10:1–16
40. Razavi N, Van Hooreweder B, Berto F (2020) Effect of build thickness and geometry on quasi-static and fatigue behavior of Ti-6Al-4V produced by electron beam melting. Addit Manuf 36:101426
41. Basha S, Venkaiah N, Sankar M (2023) Development and performance evaluation of galactomannan polymer based abrasive medium to finish atomic diffusion additively manufactured pure copper using abrasive flow finishing. Addit Manuf 61:103290
42. Huang A-N, Kuo H-P (2017) CFD simulation of particle segregation in a rotating drum. Part I: Eulerian solid phase kinetic viscosity. Adv Powder Technol 28:2094–2101
43. Cariapa V, Park H, Kim J, Cheng C, Evaristo A (2008) Development of a metal removal model using spherical ceramic media in a centrifugal disk mass finishing machine. Int J Adv Manuf Technol 39:92–106
44. Dražumerič R, Badger J, Roininen R, Krajnik P (2020) On geometry and kinematics of abrasive processes: the theory of aggressiveness. Int J Mach Tools Manuf 154:103567
45. Hashimoto F, Yamaguchi H, Krajnik P, Wegener K, Chaudhari R, Hoffmeister H-W, Kuster F (2016) Abrasive fine-finishing technology. CIRP Ann 65:597–620
46. Malkorra I, Souli H, Claudin C, Salvatore F, Arrazola P, Rech J et al (2021) Identification of interaction mechanisms during drag finishing by means of an original macroscopic numerical model. Int J Mach Tools Manuf 168:103779
47. Miller M, Bobko C, Vandamme M, Ulm F-J (2008) Surface roughness criteria for cement paste nanoindentation. Cem Concr Res 38:467–476
48. Kim JY, Lee JJ, Lee YH, Jang JI, Kwon DI (2007) Effects of rough surface on contact depth for instrumented microindentation using spherical indenter. Solid State Phenom 124:1337–1340
49. Kim J-Y, Kang S-K, Lee J-J, Jang J-i, Lee Y-H, Kwon D (2007) Influence of surface-roughness on indentation size effect. Acta Mater 55:3555–3562
50. Hyun S, Robbins MO (2007) Elastic contact between rough surfaces: effect of roughness at large and small wavelengths. Tribol Int 40:1413–1422
51. Pei L, Hyun S, Molinari J-F, Robbins MO (2005) Finite element modeling of elasto-plastic contact between rough surfaces. J Mech Phys Solids 53:2385–2409
52. Hassan N, Lee J, Kim M, Kim U, Kim M, Moon S et al (2024) Enhanced mechanical properties of aluminum nitride-yttria ceramics through grain refinement by pressure assisted two-step sintering. J Eur Ceram Soc 44:831–840
53. Karabulut Y, Kaynak Y, Sharif S, Suhaimi M (2022) Effect of machining and drag finishing on the surface integrity and mechanical properties of Inconel 718 alloys fabricated by laser powder bed fusion additive manufacturing. Materialwiss Werkstofftech 53:109–118
54. Ling J, Huang D, Bai K, Li W, Yu Z, Chen W (2021) High-throughput development and applications of the compositional mechanical property map of the β titanium alloys. J Mater Sci Technol 71:201–210
55. WEN Z-h LIN, H-q CHEN, W-m, Kewu B (2023) ZHANG L-j. High-throughput exploration of composition-dependent elasto-plastic and diffusion properties of refractory multi-element Ti-Nb-Zr-W alloys. Trans Nonferrous Met Soc China 33:2646–2659
56. Ni W, Cheng Y-T, Lukitsch MJ, Weiner AM, Lev LC, Grummon DS (2004) Effects of the ratio of hardness to Young's modulus on the friction and wear behavior of bilayer coatings. Appl Phys Lett 85:4028–4030
57. Davoodi F, Atapour M, Ashrafizadeh F, Rikhtehgaran R (2022) Dry sliding wear characteristics of NiP/TiN duplex coated aluminum alloy and wear analysis using response surface method. J Mater Eng Perform 31:6360–6372

58. Kaynak Y, Tascioglu E (2020) Post-processing effects on the surface characteristics of Inconel 718 alloy fabricated by selective laser melting additive manufacturing. Progress Additive Manuf 5:221–234
59. Mediratta R, Ahluwalia K, Yeo S (2016) State-of-the-art on vibratory finishing in the aviation industry: an industrial and academic perspective. Int J Adv Manuf Technol 85:415–429
60. Aniołek K, Kupka M, Barylski A (2016) Sliding wear resistance of oxide layers formed on a titanium surface during thermal oxidation. Wear 356:23–29
61. Jia J, Han S, Yang G, Cheng L, Yang X, Zuo J et al (2022) Response of tribological behaviors to microstructural characteristics of Ti-40Al-10V alloy at high temperatures. Tribol Int 175:107800
62. Hua K, Tong Y, Zhang F, Wang C, Kou H, Wu H, Wang H (2022) Dependence of fretting wear on the microstructure characteristics and impact on the subsurface stability of a metastable β titanium alloy. Tribol Int 165:107351
63. Guo X, Zhang J, Chen B, Li J (2020) Effects of triple heat treatment on microstructure and the dry sliding wear of TC21 titanium alloy. IOP Conf Ser Mater Sci Eng 768:022067
64. Abouelela K, Elshaer R (2022) Influence of microstructure features on wear behavior of Ti-6Al4V alloy. Int J Mater Technol Innov 2:60–66
65. Li Y, Wang X, Yang S, Hou L, Wei Y, Zhang Z, Yang X (2019) Investigation on wear behavior of cryogenically treated Ti-6Al-4V titanium alloy under dry and wet conditions. Materials 12:2850
66. An Q, Chen J, Tao Z, Ming W, Chen M (2020) Experimental investigation on tool wear characteristics of PVD and CVD coatings during face milling of Ti6242S and Ti-555 titanium alloys. Int J Refract Met Hard Mater 86:105091
67. Guglielmi P, Davoodi F, Palumbo G, Carbone G (2024) Tribological behaviour of microindented 100Cr6 steel surfaces in dry contact conditions. Int J Adv Manuf Technol 133:1–20
68. Tang W, Zhou Y, Zhu H, Yang H (2013) The effect of surface texturing on reducing the friction and wear of steel under lubricated sliding contact. Appl Surf Sci 273:199–204
69. Cao R, Yang J, Luo J, Xie X (2025) Effect of linear and staggered surface texture patterns on the tribological performance of M50 steel. Surfaces 8:78
70. Rosenkranz A, Costa HL, Baykara MZ, Martini A (2021) Synergetic effects of surface texturing and solid lubricants to tailor friction and wear–a review. Tribol Int 155:106792
71. Woźniak A, Bialas O, Adamiak M, Hadzima B, Szewczenko J (2024) The influence of laser texturing on the tribological behavior of titanium alloy Ti6Al4V in medical applications. Archives Civil Mech Eng 24:146
72. Xavier LM, Neto CA, Marins AA, Strey NF, Boher C, Scandian C (2024) Rotary barrel tumbling as a method of surface preparation for pin-on-disc wear testing samples. Surf Topogr Metrol Prop 12:035028
73. Grigoriev SN, Metel AS, Tarasova TV, Filatova AA, Sundukov SK, Volosova MA et al (2020) Effect of cavitation erosion wear, vibration tumbling, and heat treatment on additively manufactured surface quality and properties. Metals 10:1540
74. Yetim A (2010) Investigation of wear behavior of titanium oxide films, produced by anodic oxidation, on commercially pure titanium in vacuum conditions. Surf Coat Technol 205:1757–1763
75. Fagan R, Synnott DW, McCormack DE, Pillai SC (2016) An effective method for the preparation of high temperature stable anatase TiO_2 photocatalysts. Appl Surf Sci 371:447–452

Publisher's note Springer Nature remains neutral with regard to jurisdictional claims in published maps and institutional affiliations.